IEEE Access
Multidisciplinary | Rapid Review | Open Access Journal

Received November 25, 2021, accepted December 17, 2021, date of publication December 23, 2021,
date of current version January 5, 2022.

Digital Object Identifier 10.1109/ACCESS.2021.3137897

Comprehensive Design and Analysis of an Interior Permanent Magnet Synchronous Machine for Light-Duty Passenger EVs

GILSU CHOI[1], (Member, IEEE), AND GERD BRAMERDORFER[2], (Senior Member, IEEE)
[1]Department of Electrical Engineering, Inha University, Incheon 22212, South Korea
[2]Department of Electrical Drives and Power Electronics, Johannes Kepler University Linz, 4040 Linz, Austria

Corresponding author: Gilsu Choi (gchoi@inha.ac.kr)

This work was supported in part by a research grant from Inha University; in part by the BK21 Four Program funded by the Ministry of Education (MOE), South Korea; and in part by the National Research Foundation of Korea (NRF) grant funded by the Korean Government [Ministry of Science, ICT & Future Planning (MSIP)] under Grant 2021R1F1A1048754.

ABSTRACT This paper presents a detailed process for the design of interior permanent magnet synchronous machines (IPMSMs) for electric vehicle (EV) applications. First, a comprehensive design process featuring two objectives and three constraints is proposed to realize an optimal IPMSM design that can satisfy the key performance requirements for an EV application. The objectives and constraints were carefully selected and designed to obtain a balance between performance, efficiency, and cost. Because the inductances and magnet flux linkage of the machine are key design parameters for attaining optimal flux-weakening capability, the impact of the machine dimensions on these two parameters is thoroughly investigated and explained using both analytical and numerical techniques. Additional analyses including normalized key performance metrics and the impact of short-circuit faults in PM machines with three different characteristic current values (1, 1.3, and 2.6 pu) are also provided, highlighting the advantages and limitations of the three baseline designs.

INDEX TERMS Electric machine design, electric vehicle (EV), finite element analysis (FEA), flux-weakening (FW), interior permanent magnet synchronous motor (IPMSM), traction motor.

I. INTRODUCTION

Electric vehicles (EVs) have attracted significant attention worldwide over the last decade because they offer the possibility of zero tailpipe emissions and superior fuel economy. A key principle component responsible for the propulsion of an EV is the traction machine that delivers mechanical power to the wheels, as illustrated in Fig. 1. Of the many different types of traction machines, interior permanent magnet synchronous machines (IPMSMs) are being used in most EVs in the market owing to their excellent performance characteristics, including their high power density, high efficiency, and wide constant-power speed range (CPSR) [1]–[4]. In contrast to conventional electric machines, a traction machine has particular requirements that would have to be carefully addressed during the design stage. For example, several key torque/power requirements, as shown in Fig. 2, must be met over a wide speed range to improve driving satisfaction and minimize energy consumption. In addition, weight reduction is generally considered one of the key design goals to further improve the energy efficiency and cost effectiveness. Advancements in the quality of materials and thermal management have enabled IPMSMs to be downsized [1]. Additional downsizing of IPMSMs was successfully achieved by adopting a higher ratio of the reduction gear, requiring more frequent operations in the flux-weakening (FW) regimes [5]. Consequently, the importance of the FW capability for IPMSMs at high speed is becoming more significant. The high-speed performance of the machine can be improved when the characteristic current I_{ch} is equal to the rated current (i.e., $I_{ch} = 1$ pu) [6], [7]. In addition to the excellent FW capability, the $I_{ch} = 1$ pu condition is also favorable for mitigating fault effects under short-circuit (SC) conditions, because the key design parameters for reducing the SC fault current are the machine inductances and characteristic currents [8], [9].

The associate editor coordinating the review of this manuscript and approving it for publication was Wei Xu.

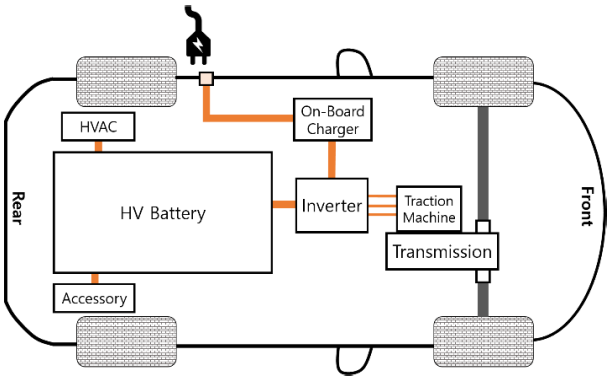

FIGURE 1. EV powertrain diagram.

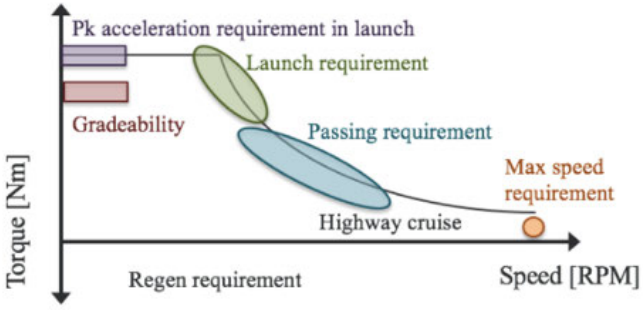

FIGURE 2. EV performance requirements.

Many researchers have investigated the impact of machine parameters capable of satisfying the different requirements imposed on the performance characteristics. However, relatively limited attention has been devoted to identifying the key machine dimensions that achieve both good machine performance and ideal FW conditions. For example, two independent research groups presented possible combinations of machine parameters for the $I_{ch} = 1$ pu condition but provided little insight into how to design the machines to achieve the performance goals with regard to the electromagnetic aspects [6], [7]. Other studies led to the development of a design method to satisfy the optimal FW condition of $I_{ch} = 1$ pu together with analytical expressions for calculating the machine inductances for surface-mounted permanent magnet (SPM) machines equipped with fractional-slot concentrated windings (FSCW) [10], [11]. However, the impact of various IPM machine parameters on achieving the ideal FW conditions has not been fully addressed.

Owing to the multi-objective and nonlinear nature of electric machine design problems, finite element (FE)-based optimization techniques have been widely employed over the last couple of decades [12], [13]. Several approaches to optimize various machine topologies have been reported in the literature [14]–[17]. In addition, the total computation time required to arrive at an optimal solution has been dramatically decreased owing to enhanced computing resources and advanced modeling techniques [18], [19].

The major objectives of this paper are as follows: 1) to provide a detailed methodology for designing an IPM machine with optimal performance over standard driving cycles; 2) to present both qualitative and quantitative results on the design and selection of geometric machine parameters, with the aim of providing other researchers and engineers in practice with clear guidance and solutions that satisfy the required EV specifications; and 3) to present comprehensive results for our trade-off analysis intended to find a solution while evaluating the balance between performance, efficiency, and cost.

Most previous design optimization studies placed limited focus on analyzing in detail the machine geometry that affects the performance of traction machines. This paper proposes a new hybrid approach that combines an analytical method to effectively select design objectives and constraints with an FE-based design approach using the characteristic current of the machine to achieve vehicle-level performance optimization. The proposed approach was applied to the design of 80 kW (pk) IPM machines (see Table 1) and the results of this analysis are presented to confirm the performance of the baseline designs by investigating measures such as the FW capability, total energy consumption during standard driving schedules, and fault mitigation effects.

II. DESIGN OPTIMIZATION OF BASELINE IPM MACHINES

A. DESIGN SPECIFICATIONS

The key specifications used in this study are based on those of the Nissan Leaf, the specifications of which are reported in a technical paper [20]. The maximum operating speed was 10,390 rpm, and the corner point speed was 2,730 rpm for peak power operation, implying a 3.8:1 constant-power speed ratio. According to the same technical paper, the maximum machine efficiency of the Nissan Leaf is approximately 95% for peak power operating conditions of approximately 6,000 rpm. Based on these data, the performance specifications that were developed for the 80 kW (pk) PM machine are provided in Table 1. The required minimum value for the machine efficiency at the corner point operation (continuous) was set at 96% for full-load operation because of potential additional losses that were considered in this analysis. The coolant temperature in Table 1 is stated to be 55 °C, which falls within the realistic range for production hybrid and battery EVs with water jacket cooling.

B. BASELINE IPM MACHINES

Neglecting the stator resistance, the dq fault currents during steady-state symmetrical short-circuit faults can be expressed as [21]

$$i_d = \frac{\psi_{pm}}{L_d} (\equiv I_{ch}), \quad i_q = 0[\mathrm{A}] \tag{1}$$

where Ψ_{pm} is the magnet flux linkage, and L_d is the d-axis synchronous inductance.

The peak transient fault current can be as high as twice the steady-state fault current amplitude [8]. In addition, the amplitude of the peak fault current during single-switch

TABLE 1. Key performance specifications for Nissan Leaf.

Parameters	*Value*	*Conditions*
Max. Output Power	80 kW	18 sec, with water/glycol cooling
Rated Output Power	40 kW	At 3,800 rpm, water/glycol cooling
Max. Torque	300 Nm	80 kW at 2,780 rpm
Nominal DC Bus Voltage	360 V	
Max. Current	400 Arms	
Max. Efficiency	96 %	Corner Point Operation: 100 Nm, 3,800 rpm
Max. Speed	10,390 rpm	
Machine Temperature	150 ºC	Maximum hot spot temperature for stator and rotor
Max. Coolant Temperature	105 ºC	Max. coolant temperature inside motor
Coolant Inlet Temperature	55 ºC	Flow rate: 7 l/min

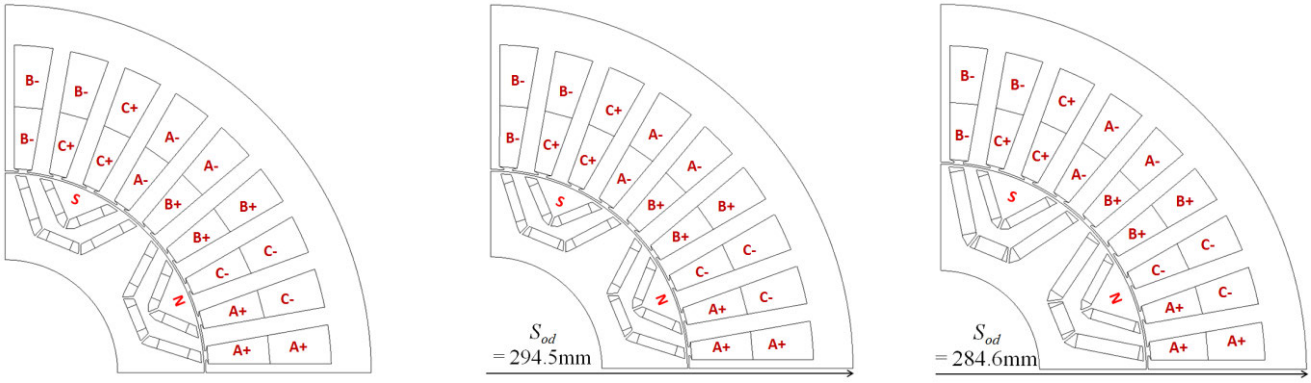

(a) I_{ch} = 1 pu (b) I_{ch} = 1.3 pu (c) I_{ch} = 2.6 pu

FIGURE 3. Cross section of baseline IPM machines rated at 80 kW (pk) @ 2,730 rpm.

TABLE 2. Key parameters of the baseline PM machines.

	I_{ch} = 1 pu	I_{ch} = 1.3 pu	I_{ch} = 2.6 pu
Stator diameter [mm]	294.5	294.5	284.6
Stack length [mm]	91	78	72
Series turns	51	51	42
Magnet mass [kg]	1.34	1.57	2.17
Total mass [kg]	40	35.6	28.4

asymmetrical short-circuit (ASC) faults can reach three times the characteristic current or higher [9]. Based on the results of these previous studies, it can be concluded that limiting the characteristic current such that it is no greater than the rated current is the single most important machine design constraint for mitigating the impact of short-circuit faults in PM machines. However, it should be noted that designs with a characteristic current higher than 1 pu have other advantageous performance metrics, such as torque density.

To provide useful comparisons, IPM machines with different characteristic current values were compared to highlight the performance characteristics of each design. Figure 3 shows the baseline 80 kW (pk) IPM machines with three different characteristic current values of 100, 130, and 260 Arms (approximately 1 pu, 1.3 pu, and 2.6 pu). The baseline machines have a 36-slot/8-pole configuration with distributed windings and two magnet layers per rotor pole. Of the many different slot/pole combinations, this specific machine configuration was selected as a baseline because of its significantly lower harmonic stator core losses and torque ripple than other configurations [22], [23].

The performance metrics for the baseline machines are summarized in Table 2, where each machine has a rotor diameter of 160 mm. Note that as the characteristic current increases, the mass of the magnet increases and the outer diameter of the stator (S_{od}) decreases because of the smaller number of turns. As a result, for the $I_{ch} = 1$ pu design, the d-axis inductance that is proportional to the square of the number of turns is increased, whereas the magnet flux

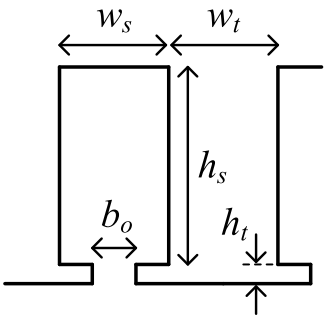

FIGURE 4. Simplified stator slot.

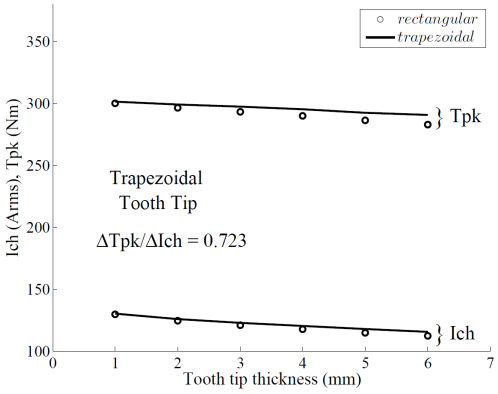

FIGURE 5. T_{pk} and I_{ch} vs. tooth-tip thickness.

linkage, which is primarily affected by the mass of the magnet, is reduced. Additional details regarding the baseline machines are presented in Section III.

III. DESIGN OF MACHINE GEOMETRY

A. STATOR DESIGN

Various combinations of machine parameters can be used to ensure that the $I_{ch} = 1$ pu condition is satisfied [6], [7]. Large machine inductances are often considered to be of key importance to comply with this condition, and details regarding the inductance calculations for FSCW-SPM machines have been reported [10], [24]. This section presents an investigation of the impact of machine geometries that were not fully covered in past work with the aim of designing a machine that satisfies the desired condition while minimizing the degradation resulting from the other important performance characteristics of traction PM machines. Both the stator and rotor parameters are carefully defined such that they are physically meaningful and dimensionless, yet using a minimum number of parameters. These features are attractive for simplifying the scaling of the design and for use in optimization algorithms that require large numbers of dimensional iterations.

The $I_{ch} = 1.3$ pu machine that was originally designed [25] was chosen as the initial design with the goal of achieving $I_{ch} = 1$ pu by modifying the machine dimensions. Given the back-emf voltage constraint, the key to further reduce the characteristic current was considered to be to increase L_d while keeping Ψ_{pm} constant, which was accomplished by increasing the stack length and reducing the mass of the magnet, as shown in Table 2. The mass of the magnet was reduced owing to changes in magnet dimensions.

The influence of the stator-side parameters, such as the slot opening, tooth-tip dimensions, and slot leakage, was first investigated while simultaneously considering the other machine performance parameters. Figure 4 shows a simplified semi-closed, parallel-sided stator slot shape to illustrate the relationship between the machine geometry and performance characteristics. The slot leakage inductance, which is key to achieving the $I_{ch} = 1$ pu condition, is proportional to the slot permeance. The slot permeance P_s and current density J for a given geometry can be calculated as follows [26]:

$$P_s = \left(\frac{h_s}{3w_s} + \frac{h_t}{b_o}\right) [\text{H/m}] \tag{2}$$

$$J = \frac{I_{pk}}{A_{slot}} = \frac{I_{pk} \cdot N_{cond}}{w_s \cdot h_s \cdot cff} [\text{A/m}^2] \tag{3}$$

where h_s is the slot height, w_s is the slot width, h_t is the tooth-tip thickness, b_o is the slot opening width in [m], I_{pk} is the peak current [A], N_{cond} is the number of conductors per slot, and cff is the copper fill factor.

The stator tooth-tip thickness (h_t) primarily controls the leakage flux. As indicated in (2), the tooth-tip thickness h_t contributes to the achievement of $I_{ch} = 1$ pu by increasing the slot permeance and, therefore, the d-axis inductance. However, an increase in h_t also decreases the torque density by reducing the useful flux linkage between the stator and rotor, and by increasing the outer diameter of the stator if the current density is constrained to be constant. The fundamentals expressed by (2) for a rectangular slot shape remain effective for the tapered slot used in the baseline machines owing to the thin tooth-tip thickness.

A parameter sensitivity study was carried out using FE analysis for tapered and rectangular-shaped tooth tips. Because the objective of this sensitivity study is to decrease I_{ch} while minimizing the reduction in torque density, the sensitivity of the peak output torque (T_{pk}) relative to I_{ch} is used for comparison. Figure 5 shows that both I_{ch} and T_{pk} decrease with increasing thickness of the tooth tip, indicating that Ψ_{pm} decreases more than L_d. The calculated sensitivity ($\Delta T_{pk}/\Delta I_{ch} = 0.723$) is lower for the tapered tooth-tip than for the rectangular-shaped tooth-tip (0.978).

The slot opening ratio (b_o/w_s) also has an impact on the characteristic current. Figure 6 shows that both I_{ch} and T_{pk} increase as the slot opening ratio increases, and the sensitivity ($\Delta T_{pk}/\Delta I_{ch}$) is relatively high. The cogging torque is also known to generally increase with large slot openings [27]. In this work, the slot opening ratio is set to be greater than or equal to 0.5, based on the results of the sensitivity study in Fig. 6, and to allow the insertion of distributed windings into the slots.

The slot width ratio, defined as $w_s/(w_s + w_t)$, primarily controls the slot leakage inductance and saturation level in

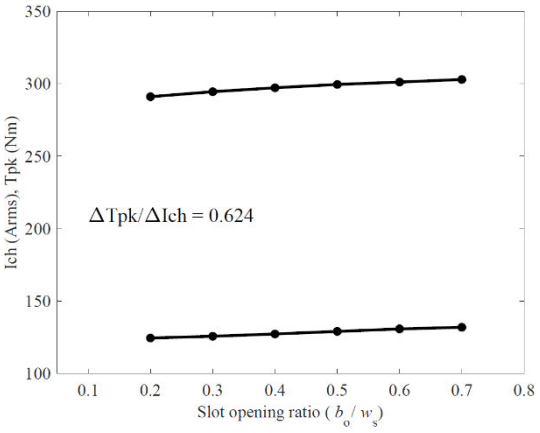

FIGURE 6. T_{pk} and I_{ch} vs. slot opening ratio.

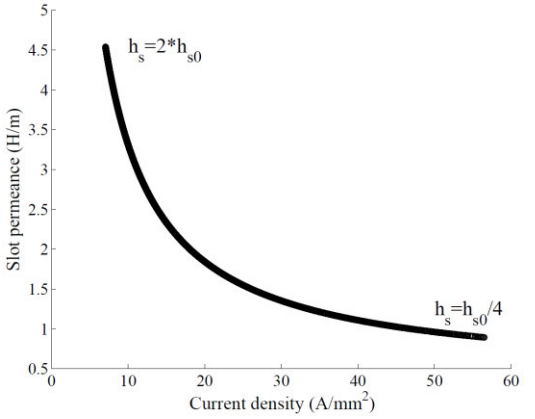

FIGURE 7. Slot permeance vs. current density (h_{s0} = 70 mm).

the stator teeth. In this study, the slot width ratio was set to 0.5, because larger ratios significantly increased the magnetic saturation in the stator teeth due to the reduction of the core area, whereas smaller values led to a high current density.

Based on the investigation presented above, the slot height (h_s) was found to be the most suitable parameter to increase the slot leakage inductance and thus achieve $I_{ch} = 1$ pu. An increase in h_s not only increases the slot permeance but also decreases the current density, as shown in Fig. 7, making it possible to apply a less sophisticated cooling system. However, this also causes the total mass to increase and thus lowers the torque density. In practice, the slot height value should be carefully determined based on the cooling capability of the system and the peak current density, which is 15 Arms/mm^2 in this study, while assuming the use of a cooling jacket for the stator.

B. ROTOR DESIGN

Figure 8 shows a cross section of the rotor of the baseline IPM machine with the key parameters identified. Owing to the complexity of the rotor cavity arrangement, rigorous analytical expressions for the rotor-side leakages were not derived

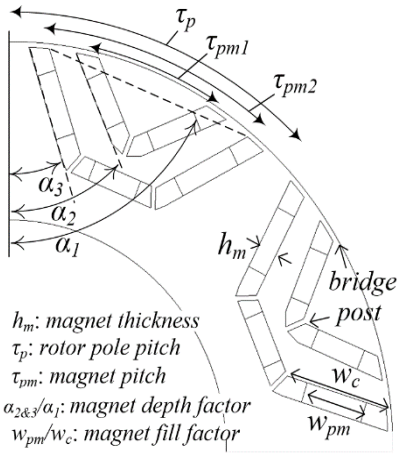

FIGURE 8. Key rotor dimensions.

in this study. Instead, a detailed explanation of the impact of the rotor geometry parameters on the machine performance is provided. The rotor-side design parameters that have a significant impact on reducing the magnet flux linkage while minimizing the average torque reduction were identified.

It is well known that the thickness of the bridge and post primarily affects the magnet flux linkage by providing leakage paths. Both I_{ch} and T_{pk} rapidly decreased as the bridge and post thickness increased, and the sensitivity ($\Delta T_{pk}/\Delta I_{ch}$) was relatively high compared to the change in the other dimensions. In an effort to minimize the reduction in the torque density as a result of an increase in these dimensions, a structural analysis was carried out using commercial FE software to find the minimum bridge and post thickness that can withstand the maximum rotor stress values at all operating speeds up to 10,390 rpm. As shown in Section IV, fillets are introduced at the cavity corners to reduce the maximum stress level by drawing the arc tangent that rounds the intersections between the two straight lines that define each of the cavity corners. Further details are provided in Section IV.

The magnet thickness (h_m) is one of the most powerful parameters for enhancing the torque density and demagnetization resistance of a machine. However, increasing this parameter significantly increases the magnet mass and machine cost.

The magnet fill factor, defined as the ratio of the magnet width w_{pm} to the rotor air cavity width w_c, primarily affects the magnet flux linkage. Figure 9 shows that both I_{ch} and T_{pk} decrease as the magnet fill factor decreases, and the sensitivity is relatively lower than that of any other rotor dimensions. One of the advantages of adjusting this variable when achieving $I_{ch} = 1$ pu is that it results in a good torque density per cost (in Nm/$) metric. This is because of the fact that the NdFeB magnets are generally the most expensive active material in high-performance PM machines. As a result of the aggressive use of this parameter to effectuate the $I_{ch} = 1$ pu condition, the total mass of the magnet of the

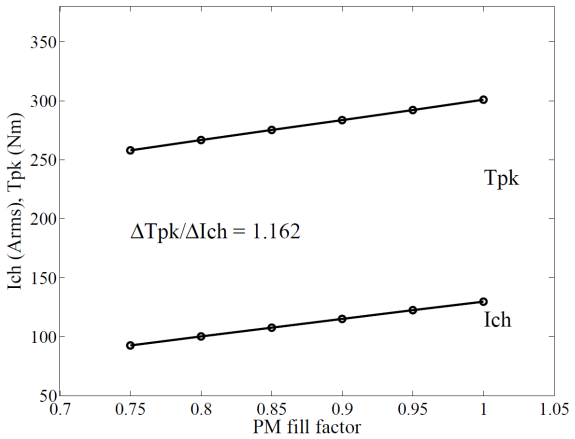

FIGURE 9. T_{pk} and I_{ch} vs. magnet fill factor.

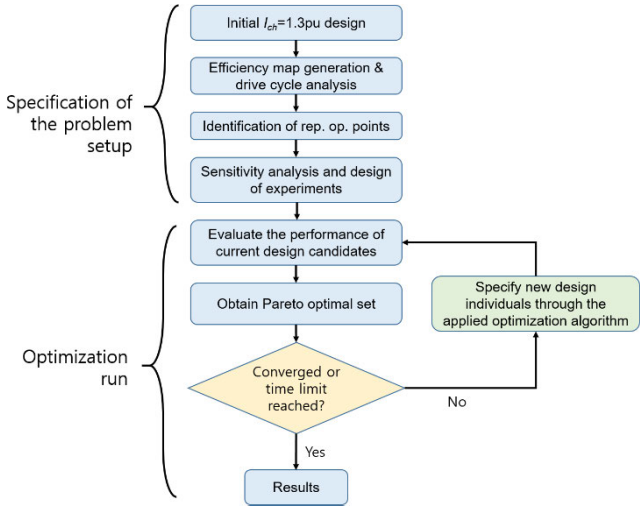

FIGURE 10. Flow chart for design process.

$I_{ch} = 1$ pu design is less than that of the $I_{ch} = 1.3$ pu and 2.6 pu machines by 15 % and 38 %.

The magnet pitch (τ_{pm}) primarily affects the rotor magnetomotive force (MMF) harmonics, the corresponding harmonic iron losses, and torque ripple [23]. Because both the iron loss and torque ripple are very important performance characteristics in traction applications, the optimal magnet pitch values presented in [23] are used as base values in an effort to minimize both the stator iron core losses and torque ripple. The magnet depth factor ($\alpha_{2\&3}/\alpha_1$) determines the radial position of each magnet layer. In general, the deeper radial position of magnets (i.e., lower magnet depth factor) allows more magnet contents to be embedded, resulting in an increase in the magnet flux linkage.

C. ELECTROMAGNETIC DESIGN OPTIMIZATION

A commercial design package (Infolytica-OptiNet) was used for the electromagnetic machine design optimization process. One of the main advantages of the optimization tool is that it

TABLE 3. Range of design variable.

	Min	*Max*	*Init. Value*
# of turns	40	54	45
Slot width ratio	0.4	0.6	0.5
Tooth-tip thickness	1 mm	3 mm	1.5 mm
PM thickness	4 mm	7 mm	6 mm
PM pitch (layer 1&2)	0.4 & 0.7	0.6 & 1	0.55 & 0.9
PM fill factor	0.7	0.99	0.85
PM depth factor (layer 1&2)	0.2 & 0.55	0.45 & 0.8	0.35 & 0.7
Stack length	70 mm	95 mm	80 mm

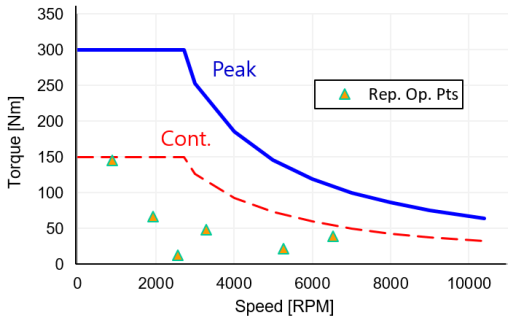

FIGURE 11. Selected representative operating points.

can find the global minimum by means of a stochastic search that modifies the machine design parameters according to an evolutionary strategy. The number of optimization variables used in this study is constrained to be a reasonably low number (i.e., 8), considering the limited computing capability available. Figure 10 shows a flowchart of the proposed design process.

During the optimization, variables evolve either in a continuous or discrete manner within the assigned lower- and upper-bound ranges. Table 3 lists the design variables and their ranges. The commercial optimization tool conducts a sensitivity study that evaluates the relative variations of the design variables from their initial values to the optimized values to determine which parameters should be prioritized to improve the design. The optimization process converged to the global minimum within an acceptable period of time. More specifically, each optimization required 900 iterations to run to completion, which required approximately 11 h when using a single desktop computer featuring eight cores.

The goal of this optimization process is to optimize the design of the 80 kW PM machine while ensuring that the requirements for key performance characteristics are met. Similar to a previous approach [28], six key operating points that exhibit the most significant energy losses during a combined driving cycle, including under both urban and highway conditions, were chosen as the representative operating points, as shown in Fig. 11. Table 4 lists the design objectives

TABLE 4. Electromagnetic design objectives and constraints.

Parameters	Variables and Value Ranges
Objectives	min { Total mass / Average shaft torque at 2,730 rpm Total energy losses over six representative operating points
Constraints	#1: 860 Vll, pk < back-emf at 10,390 rpm < 910 Vll,pk
	#2: Characteristic current values = 1 pu, 1.3 pu, and 2.6 pu
	#3: Torque ripple at rated and pk conditions < 15%
	#4: Peak current density = 15 Arms/mm^2
Variables	Number of turns, slot width ratio, tooth-tip thickness magnet thickness, magnet pitch, magnet fill factor, magnet depth factor, stack length
Constants	Rotor diameter: 160 mm; Air gap: 0.73 mm;
Material properties	Rotor magnets: VACODYM 688 TP (B_r = 1 T at 150°C), Lamination steel: M19 G29

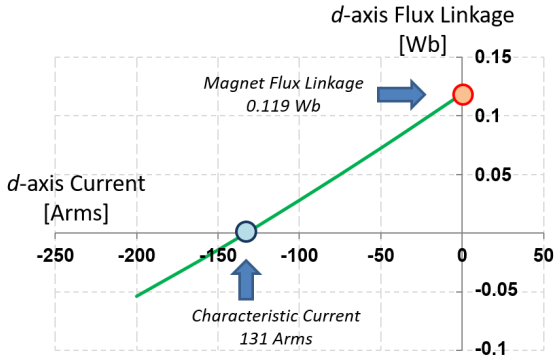

FIGURE 12. *d*-axis flux linkage vs. negative *d*-axis current.

and constraints used in the optimization process. The goal of the optimization process was to find the best possible IPM machine design that satisfy the performance specifications of the vehicle while maximizing the specific torque metric of the machine (i.e., peak torque per active material mass, Nm/kg) and minimizing the total energy losses over selected representative operating points. Similar weighting factors (i.e., 0.45 for mass per torque density and 0.55 for total energy losses, respectively) were used to balance the two objectives. The total amount of energy E_{tot} from the battery for the selected operating points can be calculated as follows:

$$E_{tot} = \sum_{i=1}^{N} \left(p_{w\_i} \frac{1}{\eta_{m\_i}} \frac{1}{\eta_{inv}} \frac{1}{\eta_g} \right) * t_{op\_i}[\mathrm{J}] \qquad (4)$$

where N is the number of representative operating points, p_{w_i} is the mechanical power delivered to the wheels for the i-th operating point, t_{op_i} is the time spent for the i-th operating point, η_{m_i} is the motor efficiency for the i-th operating point, η_{inv} is the inverter efficiency, and η_g is the gear efficiency. The motor efficiency data were generated based on an initial manual design, and a constant efficiency of 97% was assumed for the inverter and gears for simplicity. The constant efficiency assumptions were equally applied to all the baseline designs during the optimization, thus resulting in zero impact on the comparative analysis of the baseline IPM machines.

The three key constraints are the back-emf voltage amplitude at peak speed, the value of the characteristic current, and the torque ripple at the rated and peak power conditions. The back-emf voltage range at peak speed is set to ensure a balance between uncontrolled generation (UCG) vulnerability and machine torque density, and the characteristic current amplitude is set to ensure that the machine can achieve a wide CPSR and excellent FW capability. The back-emf voltage calculation can be easily integrated into the optimization by running multiple static FE simulations at no-load. The value of the characteristic current including saturation effects can then be predicted by applying an arbitrary negative d-axis current. A first-order approximation is used based on the linear relationship between the d-axis flux linkage and the negative d-axis current, as shown in Fig. 12. A similar approach using the characteristic current as an optimization goal function was reported [16].

The constraints on the amplitudes of back-emf voltage and characteristic current are well known to be closely related to mitigating the fault damages that can occur during open- and short-circuit fault conditions, respectively [21], [22].

IV. SIMULATION RESULTS

A. MACHINE CHARACTERISTICS DURING FW OPERATION

The results of our investigation of the characteristics of the FW capability and fault mitigation for baseline machines are presented in this section. Figure 13 presents the magnitude of the current and gamma angle for the baseline IPM machines during FW operation at the rated conditions, showing that the magnitude of the current is nearly the same for the three designs at a base speed of 3,800 rpm. However, the gamma angle is much smaller for the $I_{ch} = 2.6$ pu machine because of

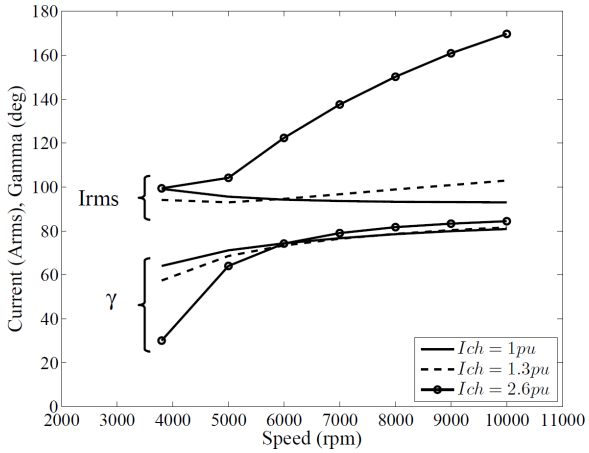

FIGURE 13. Current magnitude and gamma angle during FW operation at rated power (40 kW).

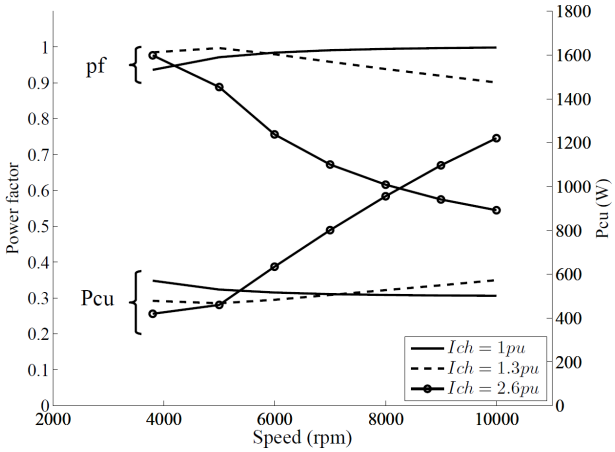

FIGURE 14. Power factor and copper losses during FW operation at rated power (40 kW).

the lower q-axis flux linkage and higher d-axis flux linkage at the rated operating condition. Because a higher negative d-axis current is required to suppress the stronger magnetic field in the $I_{ch} = 2.6$ pu design, its current magnitude begins to rise rapidly as the operating point moves into deep FW regions. As a result, the copper losses in the $I_{ch} = 2.6$ pu machine significantly increase at speeds higher than 5,000 rpm, as shown in Fig. 14. Moreover, the power factor decreases sharply for the $I_{ch} = 2.6$ pu machine beyond 5,000 rpm owing to the stronger d-axis current. Interestingly, the copper loss of the $I_{ch} = 1$ pu design decreased slightly during the FW operation. The $I_{ch} = 1$ pu design requires a relatively small d-axis current and has a relatively high saliency ratio, resulting in a reduced current magnitude above the base speed in the FW region.

B. MACHINE LOSSES AND EFFICIENCY

Figure 15 shows the predicted efficiency maps of the three baseline machines for the maximum-torque-per-ampere (MTPA) gamma angle. This efficiency comparison takes into account losses in the stator windings, iron core, and magnets. The mechanical losses and the PWM-induced losses were not calculated. These loss components that were not included are not expected to significantly change the relative efficiencies of the three machines regarding comparison purposes.

Figure 15 demonstrates that, for smaller characteristic current values, the range of the peak efficiency area (>97%) is not only extended, but the area also migrates from the high-torque, low-speed region to the relatively low-torque, high-speed region. The increase in efficiency at high speeds for a smaller characteristic current is attributed to reduced saturation. This causes reduced core losses that are dominant in the light-load operating area, together with the lower copper losses due to the decrease in the d-axis current.

TABLE 5. Peak negative d-axis current for the baseline machines after the ACS fault.

	$I_{ch} = 1$ pu	$I_{ch} = 1$ pu	$I_{ch} = 1$ pu
Value	4.2 pu	4.5 pu	6.1 pu

C. TOTAL ENERGY CONSUMPTIONS AND NORMALIZED MACHINE PERFORMANCE METRICS

The total required energy for each of the designs for three standard driving cycles (UDDS, HWFET, and US06) was calculated for the Nissan Leaf using the efficiency maps in Fig. 15. The calculated average energy consumption is presented in Fig. 16, which shows that the Wh/mile energy consumption is lowest with the $I_{ch} = 1$ pu machine, and the highest with the $I_{ch} = 2.6$ pu machine.

Figure 17 compares the machine performance characteristics based on the normalized metrics provided in the same figure. This comparison shows that the $I_{ch} = 1$ pu machine is advantageous in terms of average driving cycle efficiency, demagnetization resistance, torque ripple, and FW capability over the $I_{ch} = 2.6$ pu machine. A major downside of the $I_{ch} = 2.6$ pu machine is its required stronger stator current to achieve the same power level in the FW region, which results in higher total losses. However, the $I_{ch} = 2.6$ pu machine excels in one area; the torque density is approximately 40% greater than that of the $I_{ch} = 1$ pu machine.

D. DEMAGNETIZATION RISK

Table 5 lists the peak negative d-axis fault current values for the baseline machines after a single-phase ASC fault occurs, confirming that the fault current gradually weakens as the characteristic current weakens. Color contour plots of the poles are shown in Fig. 18 for the three baseline machines under the ASC fault. The remanence ratio (expressed in %) represents the decrease in the remanent magnetic flux density caused by the fault, and is defined as follows:

$$\left(1 - \frac{B_r}{B_{ro}}\right) * 100(\%) \tag{5}$$

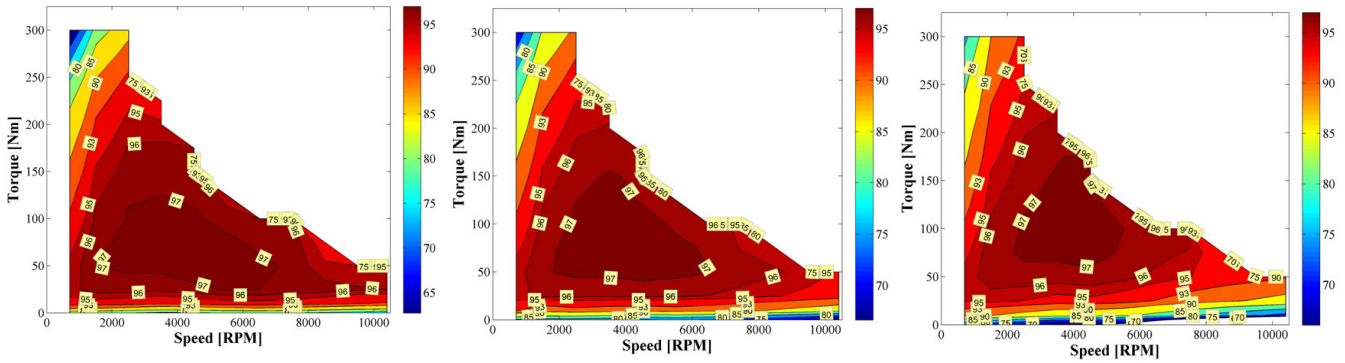

FIGURE 15. Predicted efficiency maps of the three baseline IPM machines based on MTPA at nominal Vdc.

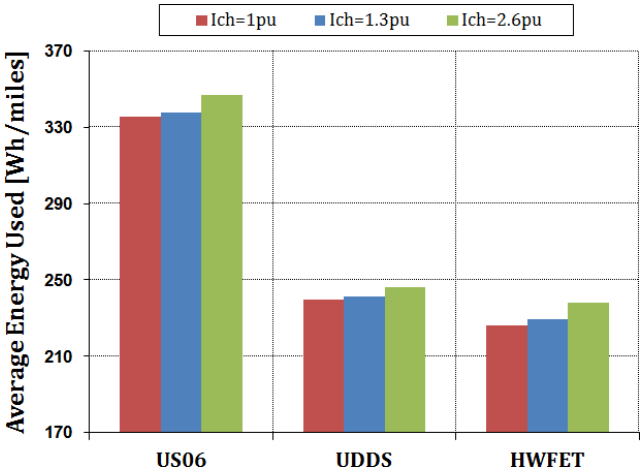

FIGURE 16. Total energy consumption during the three driving cycles.

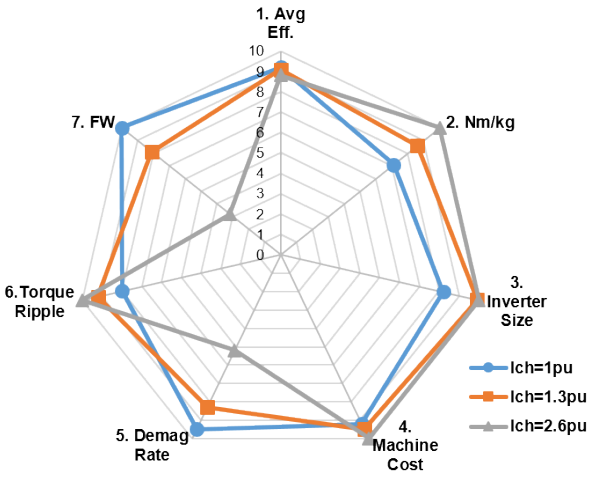

FIGURE 17. Comparisons of the normalized machine performance metrics. *Normalized performance metrics in Fig. 17:* 1. Avg. efficiency during city + highway driving schedules, 2. Peak torque per total mass, 3. 1/ Peak kVA rating, 4. Active material cost, 5. Fund. back-emf (rms) amplitude after 1-ph ASC fault, 6. Avg. torque ripple over driving schedules, 7. 1/(pu current)∗pf at rated power and peak speed.

where B_{ro} is the pre-fault magnet remanence, and B_r is the post-fault value.

The results in Fig. 18 indicate that the loss of magnet remanence for the $I_{ch} = 1$ pu machine after the ASC fault is mild compared to the other two machines, with a reduction of remanence of approx. 10% for only approx. 30% of the magnet segments. In contrast, the $I_{ch} = 2.6$ pu machine undergoes significant demagnetization with most of the magnets experiencing a 20% reduction in remanence and a 100% reduction in remanence in localized regions near the corners of the magnet. Closer inspection reveals that the $I_{ch} = 2.6$ pu machine would be exposed to considerable irreversible demagnetization even under a symmetrical short-circuit fault at no-load. Including demagnetization constraint may be considered as a further research subject.

E. STRUCTURAL INTEGRITY

Figure 19 shows the FE-predicted von Mises stress and maximum displacement that are developed when the rotor of the $I_{ch} = 1.3$ pu design is subjected to a centrifugal load at 10,390 rpm with fillets at the cavity corners, showing that the maximum stress in the rotor is lower than the permissible yield stress level of 320 MPa. Table 6 summarizes the predicted maximum principal stress and displacement for the $I_{ch} = 1.3$ pu design with and without fillets, indicating that the maximum stress can be reduced by 20 % and the corresponding displacement is reduced by 13 % by introducing the fillets. Table 6 also shows that the maximum stress in the $I_{ch} = 2.6$ pu design is at the upper end of the desired range for a long life because of the increased magnet mass, and that the amount of stress lies just inside the maximum limit.

F. NOISE AND VIBRATION

Ensuring acoustic comfort in an EV application is a complex and challenging task owing to the unique noise and vibration problems associated with EV powertrains, such as a lack of engine masking noise at low vehicle speeds and undesirable high-frequency tonal noise. In this study,

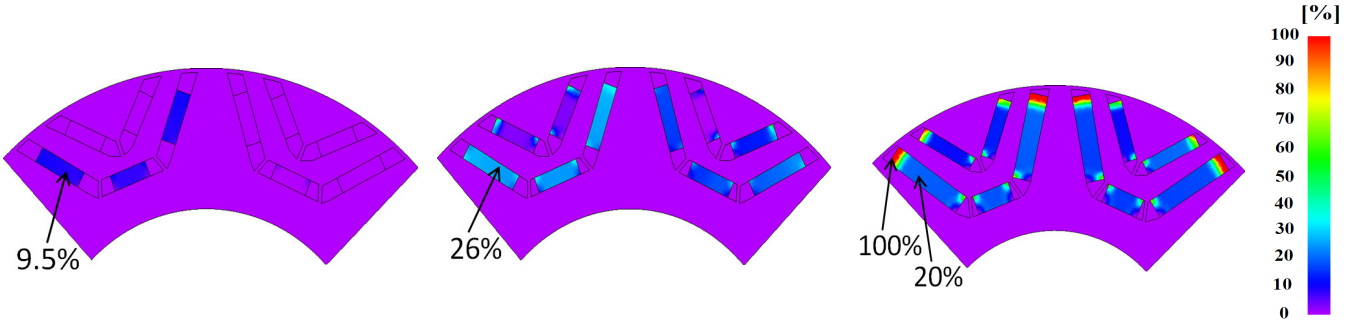

(a) I_{ch} = 1 pu (b) I_{ch} = 1.3 pu (c) I_{ch} = 2.6 pu

FIGURE 18. FE-predicted remanence ratio in baseline IPM machines after single-phase ASC fault at 180 °C.

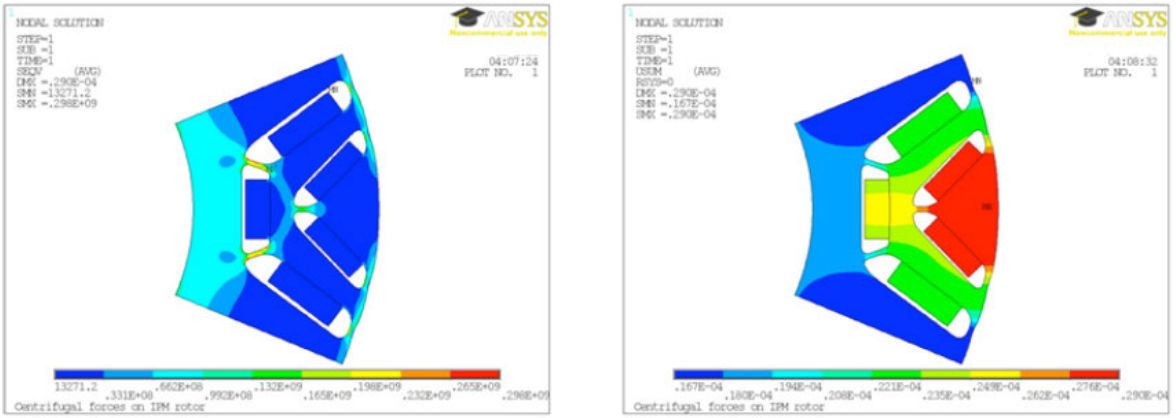

(a) von Mises stress (b) Displacement

FIGURE 19. Rotor stress and displacement of Ich = 1.3 pu design with fillets at 10,390 rpm.

TABLE 6. Calculated maximum von Mises stress and displacement at 10,390 rpm.

		Max von Mises Stress	Max Displacement
I_{ch} = 1.3 pu design	with fillets	298 MPa	28.9 μm
	without fillets	372 MPa	33.3 μm
I_{ch} = 2.6 pu design with fillets		315 MPa	30.1 μm

TABLE 7. Calculated fuel economy for 2013 Nissan Leaf with the three baseline machines including auxiliary load adjustment.

Metric	I_{ch} = 1 pu UDDS/HWFET	I_{ch} = 1.3 pu UDDS/HWFET	I_{ch} = 2.6 pu UDDS/HWFET
Avg. energy use [MPGe]	161 / 165	160 / 162	157 / 157
Adjusted MPGe incl. auxiliary load adjustment	94 / 105	94 / 103	93 / 100
Five-cycle MPGe fuel economy	100.7	99.4	97.5
EV range [miles]	71.7	70.8	69.4

the torque ripple was selected as one of the optimization constraints and was suppressed to below 15% at the rated and peak operating conditions to address the noise and vibration problems. Although the reduction in the torque ripple and the corresponding tangential forces generally contribute to smooth operation, these improvements are not necessarily directly related to the decrease in the noise and vibration in electrical machines. To effectively overcome this problem, many researchers have focused on radial magnetic forces as the main cause of electromagnetic noise in permanent magnet

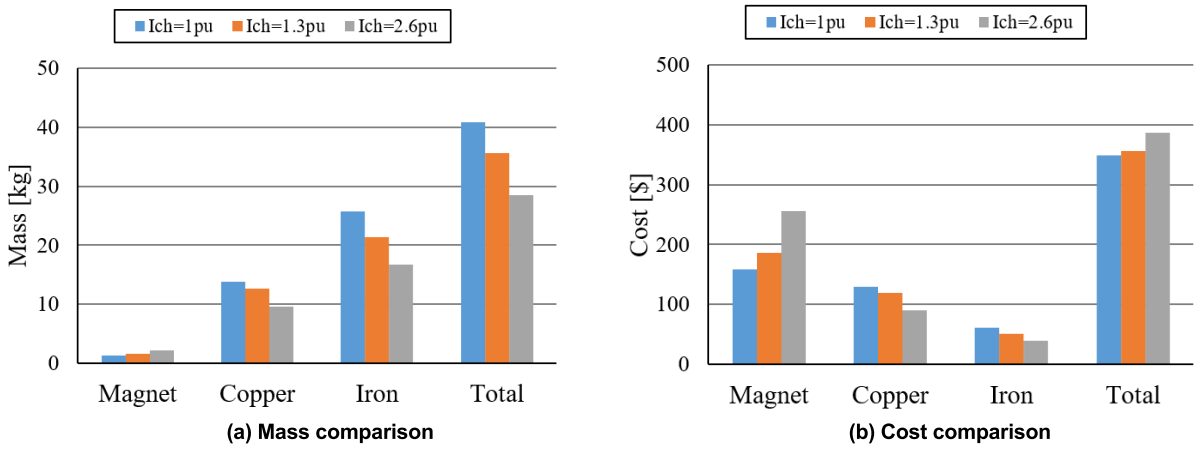

FIGURE 20. Comparison of the total mass of the machine (left) and cost (right) of the baseline IPM machines.

TABLE 8. Specific costs of active materials.

	Magnet	*Copper*	*Iron*
Cost ($/kg)	118	9.44	2.36

traction machines [29], [30]. A detailed investigation of the impact of the radial forces is beyond the scope of this study.

G. FUEL ECONOMY ESTIMATION

The simulation results were verified by calculating the estimated driving range of the EV models using the three baseline IPM designs and comparing them to the US Environmental Protection Agency (EPA) data. The auxiliary loads were assumed to be a constant power load of 400 W on the battery. In addition, 30% of the braking energy is assumed to be converted to regenerative braking.

Weighting factors were applied to the UDDS and HWFET test results to simplify the five-cycle method of the EPA, which is based on the fuel economy measurements of a vehicle across five test cycles. The equations used in [31] are as follows:

$$City\ MPGe = \frac{1}{\left(0.003259 + \frac{1.1805}{UDDS\ FE}\right)} \tag{6}$$

$$Highway\ MPGe = \frac{1}{\left(0.001376 + \frac{1.3466}{HWFET\ FE}\right)} \tag{7}$$

where UDDS FE is the calculated UDDS fuel economy in MPGe, and HWFET FE is the calculated HWFET fuel economy in the MPGe. A conversion factor of 0.02967 was used to convert MPGe to mile/kWh.

Several actual vehicle operating characteristics are considered in (6) and (7), including weather changes and higher driving aggression. The five-cycle fuel economy is expressed using weighting factors from [32], as follows:

$$5\ cycle\ FE = 0.43 * City\ FE + 0.57^{*} Highway\ FE \tag{8}$$

The values calculated using (6)–(8) are remarkably similar to the EPA sticker value for the 2013 Nissan Leaf, as shown in Table 7. Given the 24 kWh battery capacity of the Nissan Leaf, the calculated five-cycle fuel economy is comparable to a range of 71.7 miles, which corresponds well with the EPA sticker range of 73 miles. This shows that the vehicle model utilized in this study can provide acceptable fuel economy estimations.

H. COST ANALYSIS

Figure 20(a) shows that the total mass of the $I_{ch} = 2.6$ pu machine is noticeably lower than that of the other two designs. This is because the stack length is significantly reduced owing to the higher magnet content, as shown in Table 2. However, Fig. 20(b) indicates that the other two designs have a lower machine cost compared to the $I_{ch} = 2.6$ pu machine. The estimated cost comparison is based on a simple parametric study using the material costs listed in Table 8. Because the price of rare-earth materials is highly volatile owing to global supply chain issues, changes in the cost of magnets may produce different results.

I. DESIGN RECOMMENDATIONS

Based on the efficiency maps in Fig. 15, when the dominant operating regime lies in the low-speed, high-torque range and high torque density is required, the $I_{ch} = 2.6$ pu design is a more appropriate choice because of its higher specific power and increased efficiency in the low-speed region. However, if long intervals of operation in the high-speed, light-load range are required with mitigated fault characteristics for short-circuit faults, the $I_{ch} = 1$ pu design would be the best design. Moreover, the $I_{ch} = 1$ pu design was also shown to provide the basis for safe operation after triggering a crowbar overvoltage protection circuit under a UCG fault [22]. As shown in Fig. 17, the optimal flux-weakening condition can be relaxed to a higher I_{ch} value (e.g., $I_{ch} = 1.3$ pu) to improve the performance characteristics in terms of torque density, inverter size, and machine cost while

maintaining competitive performance metrics in terms of efficiency and demagnetization resistance. Note that the results of the machine cost analysis can be impacted by the price volatility of rare-earth magnets. Although the analysis is presented for a specific PM machine (36-slot/8-pole) with distributed winding configurations and two magnet layers per rotor pole, it would be applicable to any type of PM machine in a similar manner.

V. CONCLUSION

This paper presents a detailed design procedure for IPMSMs to simultaneously attain optimal FW capability and improved fault characteristics while minimizing the degradation of other important performance metrics. It is shown that the optimal FW machine with $I_{ch} = 1$ pu exhibits excellent FW performance over a wide range of constant-power operations, reduced vulnerability to SC faults, and lower overall energy consumption during standard driving schedules. Both qualitative and quantitative analyses were performed to obtain in-depth insights into the impact of key geometry parameters such as the slot dimensions, rotor air cavity dimensions, and magnet fill factor. These results yielded the ideal characteristic current and desirable performance characteristics.

After considering all of the engineering tradeoffs, the near-optimal FW machine with $I_{ch} = 1.3$ pu emerged as an attractive design owing to its promising performance metrics such as specific power, cost, and inverter sizing. FE-based structural analysis was used to predict the centrifugal forces on the rotor to ensure that the predicted maximum stress values in the rotor are within safe limits at all operating speeds up to 10,390 rpm. The torque ripple is suppressed to below 15% under key operating conditions to reduce machine-induced electromagnetic noise and vibration.

The work presented here provides a useful guideline to help engineers design IPM machines capable of satisfying the challenging performance requirements for traction applications. We plan to present more detailed work in which we address the problems associated with the mechanical properties, such as thermal and mechanical stresses, noise, and vibration, in future publications.

REFERENCES

[1] F. Momen, K. Rahman, and Y. Son, "Electrical propulsion system design of Chevrolet Bolt battery electric vehicle," *IEEE Trans. Ind. Appl.*, vol. 55, no. 1, pp. 376–384, Jan./Feb. 2019.
[2] G. Pellegrino, A. Vagati, P. Guglielmi, and B. Boazzo, "Performance comparison between surface-mounted and interior PM motor drives for electric vehicle application," *IEEE Trans. Ind. Appl.*, vol. 59, no. 2, pp. 803–811, Feb. 2012.
[3] Z. Yang, F. Shang, I. P. Brown, and M. Krishnamurthy, "Comparative study of interior permanent magnet, induction, and switched reluctance motor drives for EV and HEV applications," *IEEE Trans. Transport. Electrific.*, vol. 1, no. 3, pp. 245–254, Oct. 2015.
[4] Y. Yang, S. M. Castano, R. Yang, M. Kasprzak, B. Bilgin, A. Sathyan, H. Dadkhah, and A. Emadi, "Design and comparison of interior permanent magnet motor topologies for traction applications," *IEEE Trans. Transport. Electrific.*, vol. 3, no. 1, pp. 86–97, Mar. 2017.
[5] M. Kamiya, "Development of traction drive motors for the Toyota hybrid system," in *Proc. Int. Power Electron. Conf. (IPEC)*, Niigata, Japan, 2005, pp. 473–479.
[6] R. F. Schiferl and T. A. Lipo, "Power capability of salient pole permanent magnet synchronous motors in variable speed drive applications," *IEEE Trans. Ind. Appl.*, vol. 26, no. 1, pp. 115–123, Jan./Feb. 1990.
[7] W. L. Soong and T. J. E. Miller, "Field-weakening performance of brushless synchronous AC motor drives," *IEE Proc., Electr. Power Appl.*, vol. 141, no. 6, pp. 331–340, Nov. 1994.
[8] G. Choi and T. M. Jahns, "Investigation of key factors influencing the response of permanent magnet synchronous machines to three-phase symmetrical short-circuit faults," *IEEE Trans. Energy Convers.*, vol. 31, no. 4, pp. 1488–1497, Dec. 2016.
[9] G. Choi and T. M. Jahns, "PM synchronous machine drive response to asymmetrical short-circuit faults," *IEEE Trans. Ind. Appl.*, vol. 52, no. 3, pp. 2176–2185, May/Jun. 2016.
[10] A. M. El-Refaie and T. M. Jahns, "Optimal flux weakening in surface PM machines using fractional-slot concentrated windings," *IEEE Trans. Ind. Appl.*, vol. 41, no. 3, pp. 790–800, May/Jun. 2005.
[11] S. G. Min and B. Sarlioglu, "Analysis and comparative study of flux weakening capability in fractional-slot concentrated windings," *IEEE Trans. Energy Convers.*, vol. 33, no. 3, pp. 1025–1035, Sep. 2018.
[12] Y. Duan and D. M. Ionel, "A review of recent developments in electrical machine design optimization methods with a permanent-magnet synchronous motor benchmark study," *IEEE Trans. Ind. Appl.*, vol. 49, no. 3, pp. 1268–1275, May/Jun. 2013.
[13] G. Bramerdorfer, J. A. Tapia, J. J. Pyrhönen, and A. Cavagnino, "Modern electrical machine design optimization: Techniques, trends, and best practices," *IEEE Trans. Ind. Electron.*, vol. 65, no. 10, pp. 7672–7684, Oct. 2018.
[14] A. Cavagnino, G. Bramerdorfer, and J. A. Tapia, "Optimization of electric machine designs—Part I," *IEEE Trans. Ind. Electron.*, vol. 64, no. 12, pp. 9716–9720, Dec. 2017.
[15] A. Cavagnino, G. Bramerdorfer, and J. A. Tapia, "Optimization of electric machine designs—Part II," *IEEE Trans. Ind. Electron.*, vol. 65, no. 2, pp. 1700–1703, Feb. 2018.
[16] C. Lu, S. Ferrari, and G. Pellegrino, "Two design procedures for PM synchronous machines for electric powertrains," *IEEE Trans. Transport. Electrific.*, vol. 3, no. 1, pp. 98–107, Mar. 2017.
[17] N. Zhao and N. Schofield, "An induction machine design with parameter optimization for a 120-kW electric vehicle," *IEEE Trans. Transport. Electrific.*, vol. 6, no. 2, pp. 592–601, Jun. 2020.
[18] B. Smith, "16× speedup in ANSYS Maxwell DSO on 32-core high-performance compute farm doubles traction motor design productivity at general motors," ANSYS, MI, USA, White Paper, 2012. [Online]. Available: https://ieeeauthorcenter.ieee.org/wp-content/uploads/IEEE-Reference-Guide.pdf
[19] G. Bramerdorfer, A.-C. Zavoianu, S. Silber, E. Lughofer, and W. Amrhein, "Possibilities for speeding up the FE-based optimization of electrical machines—A case study," *IEEE Trans. Ind. Appl.*, vol. 52, no. 6, pp. 4668–4677, Nov./Dec. 2016.
[20] Y. Sato, S. Ishikawa, T. Okubo, M. Abe, and K. Tamai, "Development of high response motor and inverter system for the Nissan LEAF electric vehicle," SAE Tech. Paper 2011-01-0350, 2011.
[21] B. A. Welchko, T. M. Jahns, W. L. Soong, and J. M. Nagashima, "IPM synchronous machine drive response to symmetrical and asymmetrical short circuit faults," *IEEE Trans. Energy Convers.*, vol. 18, no. 2, pp. 291–298, Jun. 2003.
[22] S.-H. Han, T. M. Jahns, M. K. Guven, and W. L. Soong, "Impact of maximum back-EMF limits on the performance characteristics of interior permanent magnet synchronous machines," in *Proc. 41st IAS Annu. Meeting Ind. Appl.*, vol. 4, 2006, pp. 1962–1969.
[23] S. H. Han, T. M. Jahns, and Z. Q. Zhu, "Design tradeoffs between stator core loss and torque ripple in IPM machines," *IEEE Trans. Ind. Appl.*, vol. 46, no. 1, pp. 187–195, Jan./Feb. 2010.
[24] A. M. El-Refaie, Z. Q. Zhu, T. M. Jahns, and D. Howe, "Winding inductances of fractional slot surface-mounted permanent magnet brushless machines," in *Proc. IEEE Ind. Appl. Soc. Annu. Meeting*, Edmonton, AB, Canada, Oct. 2008, pp. 1–8.
[25] G. Choi and T. M. Jahns, "Design of electric machines for electric vehicles based on driving schedules," in *Proc. Int. Electr. Mach. Drives Conf. (IEMDC)*, Chicago, IL, USA, May 2013, pp. 54–61.
[26] T. A. Lipo, *Introduction to AC Machine Design*. Madison, WI, USA: Univ. of Wisconsin, 2004.
[27] Z. Q. Zhu and D. Howe, "Influence of design parameters on cogging torque in permanent magnet machines," *IEEE Trans. Energy Convers.*, vol. 15, no. 4, pp. 407–412, Dec. 2000.

[28] P. Lazari, J. Wang, and L. Chen, "A computationally efficient design technique for electric vehicle traction machines," in *Proc. 20th Int. Conf. Electr. Mach. (ICEM)*, Marseille, France, Sep. 2012, pp. 2596–2602.
[29] R. Islam and I. Husain, "Analytical model for predicting noise and vibration in permanent-magnet synchronous motors," *IEEE Trans. Ind. Appl.*, vol. 46, no. 6, pp. 2346–2354, Nov./Dec. 2010.
[30] F. Lin, S. Zuo, W. Deng, and S. Wu, "Modeling and analysis of electromagnetic force, vibration, and noise in permanent-magnet synchronous motor considering current harmonics," *IEEE Trans. Ind. Electron.*, vol. 63, no. 12, pp. 7455–7466, Dec. 2016.
[31] J. Gonder, A. Brooker, R. B. Carlson, and J. Smart, "Deriving in-use PHEV fuel economy predictions from standardized test cycle results," in *Proc. IEEE Vehicle Power Propuls. Conf. (VPPC)*, Dearborn, MI, USA, Sep. 2009, pp. 643–648.
[32] J. G. Hayes, R. P. R. de Oliveira, S. Vaughan, and M. G. Egan, "Simplified electric vehicle power train models and range estimation," in *Proc. IEEE Vehicle Power Propuls. Conf. (VPPC)*, Chicago, IL, USA, Sep. 2011, pp. 1–5.

GILSU CHOI (Member, IEEE) received the dual B.S. degree in electrical engineering from Inha University, Incheon, South Korea, and the Illinois Institute of Technology, Chicago, IL, USA, in 2008, and the M.S. and Ph.D. degrees in electrical engineering from the University of Wisconsin–Madison, Madison, WI, USA, in 2012 and 2016, respectively.

In 2020, he accepted a position with the Department of Electrical Engineering, Inha University, as an Assistant Professor. Prior to joining Inha University, he held employment at General Motors, Pontiac, MI, USA, for four years. His research interests include design and control of high-performance electric machines and drives for electrified propulsion systems. He was a recipient of the Second Prize Best Paper Award from the IEEE Industry Applications Society, in 2017. He is an Associate Editor of the IEEE TRANSACTIONS ON INDUSTRY APPLICATIONS.

GERD BRAMERDORFER (Senior Member, IEEE) received the Ph.D. degree in electrical engineering from Johannes Kepler University Linz, Austria, in 2014.

He is currently an Assistant Professor with the Department of Electrical Drives and Power Electronics, Johannes Kepler University Linz. His research interests include design, modeling, and optimization of high-performance electric machines and drives. He is an Editor of the IEEE TRANSACTIONS ON ENERGY CONVERSION and a past Associate Editor of the IEEE TRANSACTIONS ON INDUSTRIAL ELECTRONICS.